EXPERIMENT DESIGN FOR A DISTRIBUTED PROPULSION CONFIGURATION AT HIGH LIFT

J. Oldeweme*, T. Lindner†, P. Scholz†, J. Friedrichs*

* TU Braunschweig, Institute of Jet Propulsion and Turbomachinery, Hermann-Blenk-Str. 37, Braunschweig, Germany

† TU Braunschweig, Institute of Fluid Mechanics, Hermann-Blenk-Str. 37, Braunschweig, Germany

Abstract

The complexity of propeller wing interactions in a distributed propulsion (DP) configuration requires high quality wind tunnel data to fully exploit the benefit of such a configuration. Benefits of DP are most pronounced in high lift, high thrust configurations, which sets the focus for the proposed experiment. The designed wind tunnel model features a two element wing with three co-rotating propulsion units on a separate carrier that can be readily traversed and pitched relative to the wing. This enables a thorough investigation of propeller position from $0 < x/D < 1$ and $-0.25 < z/D < 0.25$, excluding nacelle effects. Experiments are conducted up to Re $= 2.9 * 10^6$ based on wing chord. The 2D wing spans 2.4 m in the closed test section of the Propulsion Test Facility, TU Braunschweig. It features an adjustable fowler flap. To avoid data contamination from side wall effects, the model is split in three sections, each representing a periodic section from an infinite DP wing. While the outboard sections provide the quasi periodic conditions but suffer from side wall effects, the centre section is instrumented. This includes angle resolved thrust and torque measurements of the drive train, internal 6K force measurement on the profile section and pressure sensitive paint on the suction side. Multiple sets of propellers with two different diameters are installed, following different design strategies. A homogeneous induced axial velocity design and a MIL propeller are compared regarding propeller wing interaction. The constant speed propellers are pitched to deliver thrust in the range of $0.07 < c_T < 0.3$ at two different advance ratios. The propellers are designed to have a constant Ma_{tip} for all operation points and a scaled D/c, J and c_T. With the proposed instrumentation plan a full set of integral parameters for drive train and wing can be measured, while keeping the configuration highly modular. Time resolved pressure measurement and time-averaged PSP allow an in depth analysis of three dimensional pressure distribution and instationary effects on the wing.

Keywords

Wind tunnel model; Distributed Propulsion; High-lift

NOMENCLATURE

Symbols

a	speed of sound	m/s
α	Angle of Attack	deg
B	Width and Height of Test Section	m
C_T	Thrust coefficient	
D	Propeller Diameter	m
J	Advance ratio	
n	Rotational speed	1/min
ρ	Density	kg/m^3
T	Thrust	N
V_∞	Inflow Velocity	m/s
I	Measured Intensity	counts
Tu	Turbulence level	%

Indices

$_0$	Wind-Off Condition
$_h$	Hub

Abbreviations

BEMT	Blade Element Momentum Theory
CIRA	Centro Italiano Ricerche Aerospaziali
DC	Direct Current
DEP	Distributed Electric Propulsion
DP	Distributed Propulsion
OP	Operation Point
PSP	Pressure Sensitive Paint
PTF	Propulsion-Test-Facility

doi: 10.25967/570125

1. INTRODUCTION

The goal of making aviation more environmentally friendly means that new drive concepts are increasingly becoming the focus of research. New possibilities in the field of electric motors enable the approach of distributed electric propulsion [1, 2]. Propeller-wing interactions have been studied intensively. Especially in the field of propeller aerodynamics and interactions of propellers located at the wingtip [3–5]. The interactions between propellers of a DP system were experimentally measured in the forward flight configuration by de Vries [6]. However, the positive effects of DP can increase the performance of the system especially in high-lift systems, through positive propeller-wing interactions, as Deere shows numerically [7, 8]. Patterson does a conceptual design of such high-lift propeller systems. [9]. As already shown by Veldhuis, different parameters for example the relative propeller position of the wing can change the interaction of propeller and wing [10].

The Clean Sky 2 project CICLOP does research on the high-lift aspect of distributed propulsion. This project is carried out by the Technische Universität Braunschweig in cooperation with the Italian Aerospace Research Centre (CIRA). The overall objective of this experiment design is to provide high fidelity experimental data of aerodynamic effects and characterisation for closely coupled distributed propulsion. The most significant parameters that have either a positive or negative aerodynamic effect will be identified and quantified. Parameters that are studied by this setup are

(a) the propeller design parameters (size, thrust, advance ratio, blade loading and local blade loading distribution, design strategy)
(b) the coupling between propeller and wing (relative horizontal and vertical propeller position to wing, spanwise propeller position, inclination angle)
(c) the wing high-lift performance (flap setting, leading edge design)

The experiment design allows studying all of the above effects using a DEP configuration with a wing in high-lift configuration and three propulsion units on a separate carrier creating fully realistic unsteady flow conditions. In combination with high-accuracy and time resolving instrumentation in wing and propeller, the relevant aerodynamic effects are identified to allow a comprehensive high-fidelity sensitivity analysis. The objectives for the scientific analysis in this experiment are a detailed characterisation of the aerodynamic influences of a close-coupled operation for both, the propellers and the high-lift wing.

2. WIND TUNNEL MODEL

The DEP-model of CICLOP (Characterisation of the Interaction between wing and Closely Operating Propeller) is installed in the Propulsion Test Facility (PTF) of the Institute of Jet Propulsion and Turbomachinery, shown in Figure 1. The facility is an atmospheric wind tunnel (Eiffel configuration), where the flow enters the test section via the inlet tower and corner vanes, with screens and a honeycomb improving the quality of the flow. The motor gearbox shown in the Figure which is normally used to power propulsion units is not used in this setup. The maximum speed of $Ma = 0.20$ is reached in the rectangular $2.4\ m * 2.4\ m$ test section, where the DP-model is located. The turbulence level is $Tu < 0.05\ \%$ for all operation conditions.

The whole model, including three propellers and the wing is rotated along a common shaft at $x/c = 0.36$ in the centre of the wing. The height of the rotation axis sits at $z/B = 0.08$ below the symmetry plane of the test section, allowing for a centred position of the propellers at moderate angle of attack. Due to the geometry of the closed test section, a range of $-10° < \alpha < 22°$ is possible. Downstream of the model, corner vanes lead the flow towards the outlet tower [11]. Not used in this experiment but noteworthy is the crosswind capability of the PTF, effectively generating a slip angle without yawing the model in the test section.

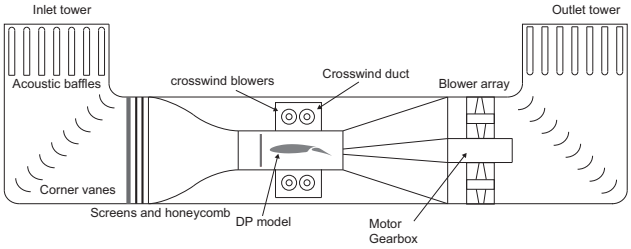

FIG 1. Layout of the PTF, wing not to scale [11]

The overall structure of the design is shown in Figure 2. The model is connected to load bearing structure of the wind tunnel via a steel frame (a). In this space are two geared servo motors, capable of pitching the whole model in wind on conditions. The sideplates (b) connect three propellers (c) to the wing (d). They extend downstream to allow the mounting of additional ballast plates, keeping the overall pitching moment moderate. The special feature of this design is that the propulsion units are not fixed to the wing and instead are located in front of it on a additional support structure. In this manner, the complex propeller wing interaction can be investigated, omitting secondary effects that come with nacelle integration. The drive units are located on height-adjustable solid and hollow tubes so that the relative vertical position to the wing can be changed (e). Additional cross bars provide more strength. These must be modified if the height is to be adjusted. The height setting is mounted on two longitudinal carriers (f). The propulsion units can be moved on these carriers so that the spanwise position can be varied. The carriers are fixed to the side walls with two profiles (g). On these profiles, the carriers can be shifted in order to change the horizontal distance from all units to the wing. By rotating a carrier and exchanging the spacers, an inclination angle can also be set. This modular setup allows a fast change in configuration, exploiting the full potential of the DEP configuration. To avoid possible damage, two vibration sensors of type VSA05 from IFM electronic are attached

to each unit to monitor the vibrations in two directions. The VSE100 is used as a diagnostic device.

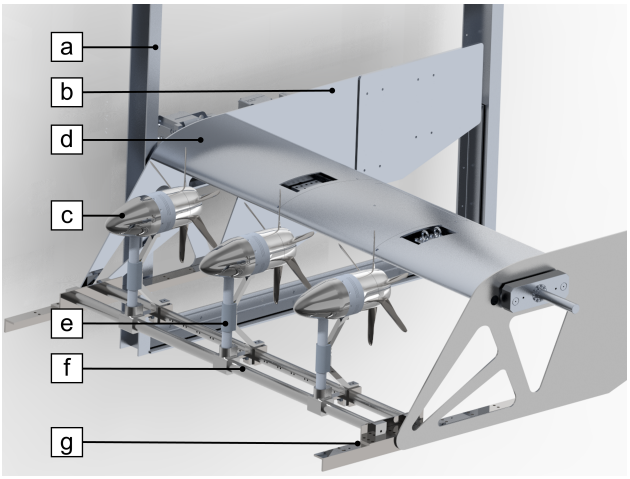

FIG 2. Experiment design: Steel frame, three propulsion units, wing and connecting sideplates

2.1. Wing

The wing features a $15.3\ \%$ thick airfoil with $2\ \%$ camber and a fowler flap. The profile design was performed by CIRA in scope of the IRON Project. The nominal chord length for the retracted flap is $c = 0.8\ m$, resulting in operating conditions between $Re = [2.1\ ...\ 2.9] * 10^6$ in the atmospheric wind tunnel. Tripping tape at $0.05\ x/c$ will ensure fully turbulent flow on both flap and main element. The flap is adjusted on thin steel brackets. Two of these brackets are on each section of the wing. This carrier is designed to have less than 0.5 mm deflection at maximum flap loading, ensuring precise positioning of the sensitive gap. The focus of the experiments will be the take-off configuration with $20°$ flap deflection as shown in Figure 3.

The whole wing is split in three different spanwise sections: The centre section is located behind the centre propeller unit, such that it is effectively a quasi-periodic element, where the role of the two outer sections is merely to generate this periodicity. Therefore, most instrumentation for both wing and propellers are focused on the centre elements. It is mechanically decoupled from the outer wing sections and sits on an internal balance. The $0.875\ y/c$ wide section thereby represents a periodic wing section of co-rotating propellers. The gap towards the outboard wing sections is minimised by sanding intermediate blocks of wing section in-situ, reducing the remaining gap to $y/c < 0.1\%$.

By this means wind tunnel interference of the closed test section is partially circumvented. However, RANS calculations near stall have shown that preliminary stall cells develop in the side-wall corners. Their displacement accelerates and straightens flow in the centre section, delaying separation compared to 2D results. To mitigate this effect, retrofitted droop-nose type wing extensions in the outboard section with a spanwise extent of $y/B = 0.375$ are foreseen. The design goal is keeping sectional circulation $\Gamma(y)$ constant by decambering the profile, while unloading the pressure distribution by extending the wing. A secondary requirement is minimal surface deflection of the model. This is not only important for maintaining the desired airfoil shape, but also for the optical measurements mentioned in Section 2.3. At maximum expected loading based on MSES calculations, the deflection in the centre part of the wing peaks at $< 8\ mm$ as per finite element simulation. The overall design is a compromise of model mass and stiffness. To limit torsion under aerodynamic load, the angle of attack is driven on both sides of the wing.

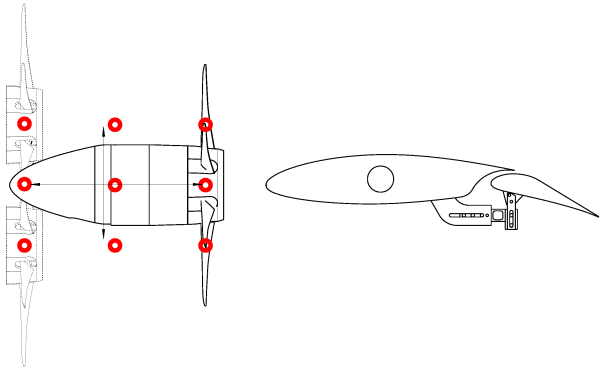

FIG 3. Red dots indicate the range of possible propeller positions in front of the wing, shown here in take-off configuration.

In Figure 3 a cross section of the wing, flap, flap bracket and the rotation axis is shown. The red dots indicate the possible positions of the intersection of rotation axis and propeller root. Full lines represent the closest coupled centre position. Refer to Table 4 for the range of relative motion.

2.2. Propulsion

The three propulsion units consist of a six-bladed propeller. For this experiment, three different propeller blades were designed by CIRA. Blade A and B have a tip diameter $D = 0.6\ m$ with a hub diameter $D_h = 0.1896\ m$. The difference between the two blades is the design strategy. While blade A was designed conventionally for minimum induced losses (MIL), blade B was designed for a constant radial output velocity. The homogeneous wake of propeller B is subject of analysis for an improved propeller-wing interaction in DP. Blade C is smaller with $D = 0.4\ m$ and $D_h = 0.1308\ m$ and is like blade A a MIL blade. The blades were designed using the BEMT method. Further details on this design process can be found in the corresponding publications by Pagano [12] [13]. All blades are made of high-strength 34CrNiMo6 steel. The aerodynamic design of the layout merges into the propeller root via a transition section as shown in Figure 4. The propeller blade roots and the propeller hub were designed to allow different pitch angles for each blade to be adjusted individually. Therefore, the blade roots and their matching parts in the propeller hub are conically shaped. The

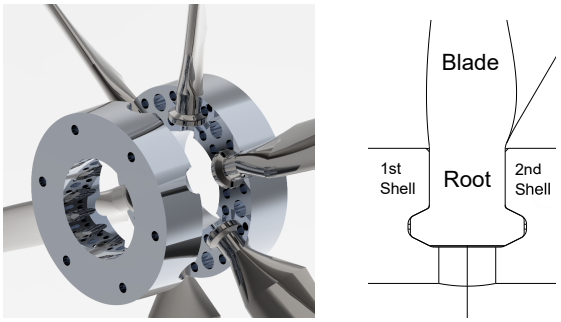

(a) (b)

FIG 4. Clamping of the propeller blades

propeller hub consists of two parts, with the connecting surface in the propeller plane. Each propeller blade is fastened with four screws. Figure 4 (b) shows the clamping structure of the propeller blades. The propeller blades are pitched individually. A tool was developed for this purpose as part of the TU Braunschweig project *Bürgernahes Flugzeug*, which is adapted to the changed dimensions [14]. The tool is screwed to the front of the hub shell. At a radial height of $r/R = 0.75$, two probe tips are located which are pressed against the pressure side of the blade. Using a feeler gauge, the angle can be adjusted with an accuracy of up to $1/10°$. This procedure allows the angle to be set precisely for each individual blade, which may not be possible with central adjustment.

Due to the two different diameters of the propeller blades, two different drive trains are necessary. In both cases, the basic power train is the same and is shown in Figure 5.

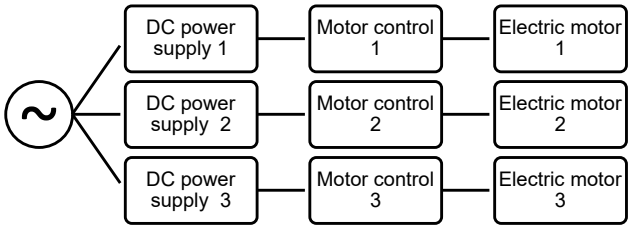

FIG 5. Power supply of electric motors.

Permanent-magnet motors are used in both drive trains. They are originally designed for application with batteries. For ease of measurement they are substituted with DC laboratory power supplies in this wind tunnel experiment. The power electronics of both drive trains differ in their components not only with respect to geometric dimensions, but also with respect to performance-related requirements (refer to 4). Therefore the power components differ between the large and small drive trains.

Large drive train

The electric motor of the large drive train for blades A and B is the EMRAX 188 HV CC. The motor control used to achieve all the desired operating points is the BAMOCAR-PG-D3-700-400-IN from Unitek. With 52 kW peak power, a maximum at $90\ Nm$ Torque and up to 8000 RPM the motor can perform all operation points that a planned. The motor diameter of $188\ mm$ is almost a third of the propeller diameter, which finally dictated the rather large hub ratio of the whole unit. The technical characteristics of the motor is summarised in Table 1. As already mentioned, the control in this experiment is not connected to a battery but to a DC laboratory power supply from ITECH for each motor control. For this drive train, the power supplies are the bi-directional IT6018C-800-75. Wind milling is not planned with this setup and should be avoided by the operational process. However, in the event of an unforeseen circumstance this type of devices will not get damaged. For each drive train a master and a slave unit are used to achieve the full potential of the motor. The design of the large drive train is shown in Figure 6. In the core of the unit is the Emrax

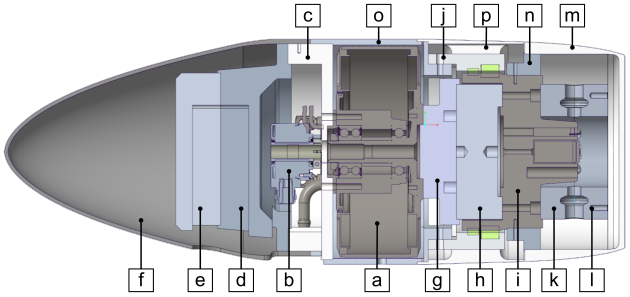

FIG 6. Large drive train.

motor (a), which is an outrunner. The encoder (b) is attached to the static backside of the motor. The encoder is necessary to measure the rotational speed and angular position of the motor. Next to the encoder the phase cables and the water cooling system are located. The motor connection (c) is also mounted on the backside of the motor. This has a cut-out for the cables and water tubes. The mounting brackets (d,e) are attached to the motor connection. Between these, a rectangular profile is clamped which is fixed to the height adjustment of the superstructure. The spinner (f) attached to the motor connection is static and provides an optimal inflow. On the rotating part of the frontside of the motor, after an adaptor plate (g), sits the measuring flange (h). Via the attached telemetry hub (i), the data from the measuring flange are transmitted between the telemetry hub and the electronic ring (j) by using a coil system. The electronic ring is static due to the attachment with the motor connection. Since only the centre propeller has instrumentation, there is a dummy component in place of the measuring flange and the telemetry hub in the outer two units. The two hub shells (k,l) are mounted on the telemetry hub. As can be seen, the propeller plane is located as far downstream of the unit as possible to allow positions as close as possible to the wing. The spinner (m), which is connected to the hub via the spinner support (n), is therefore also shortened with a clear separation edge. There is a recess in the spinner for each propeller blade. A counterpart to the spinner keeps the gap as small as possible for different pitch angles. Between the stator (o) and the spinner is an aerodynamic cover (p).

Parameter	Emrax	Plettenberg
Motor diameter in mm	188	131
Motor length in mm	98.5	132
Weight in kg	7.2	3.1
Cooling	Water and Air	Water
Power in kW	max. 52	max. 15
Rot. speed in 1/min	max. 8000	max. 11000
Torque in Nm	max. 90	max. 40
Voltage in V	max. 430	max. 120
Efficiency max	92 % to 98 %	> 90 %

TAB 1. Motor data of EMRAX 188 HV CC and Plettenberg NOVA 15/50/B4 S P30 HF.

Small drive train

The electric motor of the small drive train for blade C is the Plettenberg NOVA 15/50/B4 S P30 HF. The control used to achieve all the desired operating points comes from the motor manufacturer itself and is the MST140-200. With his 15 kW peak power, a maximum at $40\ Nm$ Torque and up to 11000 RPM the motor can perform all operation points that are planned. With a diameter of $131\ mm$ the ratio to the propeller diameter to hub is comparable to the large drive train. The technical characteristics of this motor are also summarised in Table 1. For each propulsion unit the power supplies are the ICH-IT6018C-300-225 bi-directional power supply from Itech. With a maximum voltage of $300\ V$, a maximum current of $225\ A$ and a maximum power of 18 kW, the full potential of the motor can be realised with these devices. Like the large drive train, these are also capable of regenerating electricity in case of wind milling, thereby avoiding damage in electronic components in emergency shutdown. The design of the small drive train is shown in Figure 7. In contrast to the Emrax motor, the Plettenberg motor (a) located in the centre has a rotating shaft. An adaptor hub (b) is pressed onto this shaft via a shrink disk (c). On this hub, equivalent to the large drive train, there are two hub shells (d,e), between which the propeller blades are clamped. The rotating spinner (f) is shortened as well to achieve close wing positions. The spinner and its counterpart for small gaps at various pitch angles is bolted to the adaptor hub. The stator (g) is mounted to the front of the motor and is also the external covering. The measuring flange (i) is mounted using the motor connection (h). Since also in this setup only the centre propeller has instrumentation, there is a dummy component in place of the measuring flange in the outer two units. Via another adaptor (j), the entire unit is connected to a rectangular profile with two mounting brackets (k,l).

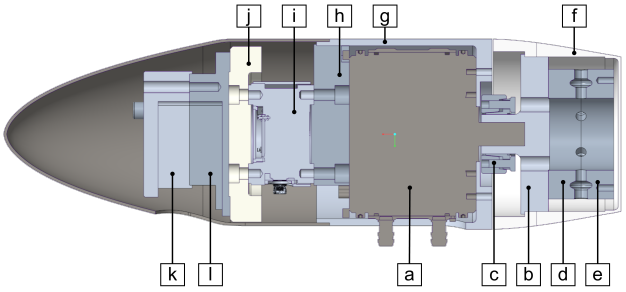

FIG 7. Small drive train.

2.3. Instrumentation

The focus of investigation lies on the quasi-periodic centre wing element as explained in Section 2.1. The centre wing section is equipped with force and pressure sensors. The three force and moment components acting on the section are measured with a RUAG 196-6O balance. It connects the centre shell, manufactured from aluminium, with the load bearing spar. It allows for a measurement design force range of $2000\ N$ in the vertical (Fz) direction and $120\ Nm$ around the pitch axis. Limit loads are significantly higher. In case of severe vibrations in test cases with flow separation the balance can be exchanged with a solid dummy piece as a backup. Additionally, the strain in the bracket connecting the flap is measured. In this way, a signal proportional to the moment and a signal proportional to the flap-lift can be extracted. Two chordwise rows of closely spaced pressure taps are placed in the wake of the propeller tips. They serve two goals: Information of profile pressure distribution in the propeller wake and in situ calibration of PSP data. For data acquisition, multiple units of Scanivalve DSA3016 with a range of $15\ psi$ differential pressure are used. Figure 8 displays their positioning, as well as a definition of the coordinate system. Here, the centre position of the drive train relative to the wing is shown (refer to Figure 2). The origin is placed in the symmetry plane on the leading edge.

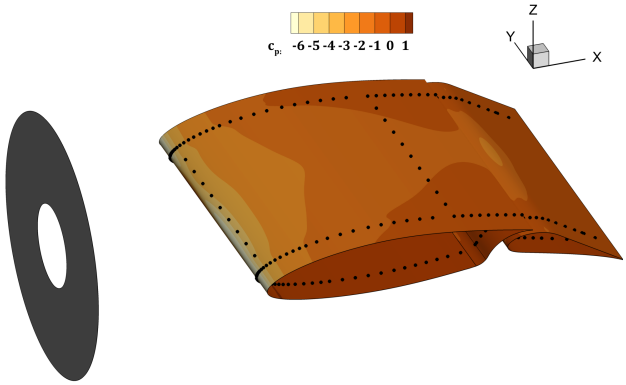

FIG 8. Black dots indicate the position of pressure ports on a preliminary RANS + Actuator Disc solution at $\alpha = 9°$

Since the three dimensional pressure distribution is of major interest, two means of measuring this are proposed. One is the use of Pressure Sensitive Paint (PSP) on the top surface, as described later. Since the resolution, sig-

nal to noise ratio and repeatability lacks behind conventional pressure measurements, a "scanning" procedure is foreseen: By shifting the whole drive train assembly laterally with respect to the wing (refer to Figure 2), the rows of pressure tabs on the wing effectively scan over the wake of the centre propeller. The combination of PSP and the scanning procedure will provide reliable data for the comparatively low dynamic pressures at $U_\infty = 40; 55\ m/s$ for PSP measurements. Less densely spaced pressure ports extend the full span of the wind tunnel model to ensure the quasi-two dimensional setup. Also, premature stall on the side wall corners will be detected by this means.
Additionally, three dynamic pressure sensors are installed on each row in order to get temporal information of the swirl induced angle of attack in the propeller wake. The ratio of pressure measured fore and aft of the suction peak ($x/c = 0.006; 0.125$) provides a signal independent of dynamic pressure in the wake. Much care was taken that these flush mounted sensors have a frequency response of $> 10\times$ blade pass frequency. This is achieved by keeping the tubing length that is sanded flush to the surface minimal. The time response is then calculated in a Bergh-Tijdeman model. With a tubing diameter of $d_i = 0.3\ mm$ a length of $1\ mm$ leading to the sensor is achieved. With an assumed internal sensor volume of $\approx 1\ mm^3$ the systems resonance frequency is well above $10\ kHz$ under atmospheric conditions.
The aluminium surface will be coated with a white base coat for PSP. Besides proper binding of the PSP, this basecoat provides a homogeneously reflective surface and chemical insulation to the metal. A biluminophore paint (ISSI Binary FIB) is used for its high accuracy and relatively robust measurement technique. The top surface of the model will be investigated, therefore the 400 nm UV-excitation lights and cameras are placed in the wind tunnel ceiling. Two PCO.4000 cameras will be used to measure the two emission spectra of the PSP. The intensity of one spectra contains the pressure information via an oxygen quenching mechanism. Since this value is also dependent on excitation intensity and temperature, the second camera records only the reference signal. In an ideal PSP formulation, this reference $R(T, E)$ has the same temperature and excitation dependency as the signal $S(p, T, E)$, thereby allowing for the formulation of the ration $I(p) = S/R$. To further compensate for inhomogenities in the PSP thickness, mixture of reference and signal molecules and model geometry, a "Ratio of Ratio" of wind-on I and wind-off image I_0 is the final step of processing. Preceding trials with the setup described above showed, that in this two-camera approach at low dynamic pressures the major error contribution is misalignment in the image registration.
The images containing pressure information are mapped onto a surface model of the wing, visualising the time-averaged pressure distribution. For calibration of the PSP the an in-situ approach is chosen. Here, the intensity ratio I/I_0 of the PSP is mapped to the known pressure values at the pressure ports, creating Stern-Volmer relations. The known position of the pressure taps are used as registration markers.
The centre propulsion unit section is to be equipped with force and torque sensors. In case of the large drive train the measuring flange, of the TU Braunschweig project *Bürgernahes Flugzeug* is reused [14]. The flange has a range of $\pm$2000 N axial Force and $\pm$270 Nm torque. These ranges are far above those to be measured with this experimental setup. In the field of values to be measured, the accuracy for the axial force is less than 0.2 % and for the torque less than 1 %. The data transmission concept using a telemetry hub and electronic ring to a transient recorder is the same. The components were newly manufactured and instrumented due to the different dimensions. For the measurement of the rotational speed as well as the angular position of the motor and thus the propeller, the encoder B58-F-12-L-720-KR20 from Waycon is used. This incremental encoder fits into the available space and can resolve the position in 0.5° due to 720 pulses. Thrust and torque are measured in the centre propulsion unit of the small drive train with a static load cell. The K6D80 from ME-Meßsysteme in the smallest version (500N/20Nm), which has been calibrated for the range to be measured, is sufficient to cover all measuring points and to withstand all loads. The GSV-8DS with eight input channels recommended by the manufacturer is used as the measuring amplifier. A data cable between the Plettenberg motor and the controller allows the rotational speed to be set at the controller and the angular position of the motor to be measured in 4° steps. Since the current motor position is lost when the control is switched off, one position information per revolution is provided by an additional laser setup.
The proposed experimental setup allows for two research goals in CICLOP. The system efficiency, resulting from the propulsive efficiency and glide ratio can be directly measured. For a given operating point the best possible propeller position can be determined. Furthermore, the PSP coating on the top surface of wing and flap will give insights to the stall mechanism in the propeller wake for the three different sets of propellers.

3. OPERATION POINTS

In the upcoming test campaign, various parameters were selected in order to generate reliable results. Three propeller configurations were determined by the three different blades. In configuration A, all three propulsion units are equipped with six A-blades each. In configuration B, the outer two units have A-blades and the centre propeller has B-blades. In configuration C, only C-blades are used. An overview of this is shown in Table 2.

	Propulsion unit		
	Left	Middle	Right
Configuration A	Blade A	Blade A	Blade A
Configuration B	Blade A	Blade B	Blade A
Configuration C	Blade C	Blade C	Blade C

TAB 2. Configurations of propulsion units.

In addition to these three configurations, two different levels of advance ratios J are analysed:

$$J = \frac{V}{n\ D}. \tag{1}$$

The blade tip mach number

$$Ma_{tip} = \frac{\sqrt{V^2\ +\ (D\ n\ \pi)^2}}{a} \tag{2}$$

of the propeller blades is set constant with $Ma_{tip} = 0.581$ in all operation points for aerodynamic comparability. Due to the different propeller diameters and the selected inflow velocities of $V = 40\ m/s$ and $V = 55\ m/s$, the rotational speed results accordingly. This results in the four basic operating points as shown in Table 3.

OP	Config	D in m	J	V in m/s	n in 1/min
1	A,B	0.6	0.649	40	6160
2	A,B	0.6	0.909	55	6050
3	C	0.4	0.649	40	9250
4	C	0.4	0.909	55	9075

TAB 3. Operation points.

Parameter	Evaluated values
Propeller Configuration	A, B, C
Advance ratio J	0.649, 0.909
Freestream velocity V_∞ in m/s	40, 55
Propeller Diameter D in m	0.4, 0.6
Rotational speed in RPM	6050, 6160 and 9075, 9250
Blade tip velocity Ma_{tip}	0.581
Rotation direction	co-rotating
Relative propeller position	
Vertical to wing z/D	$-0.25 < z/D < 0.25$
Horizontal to wing x/D	0 < x/D < 1
Inclination angle	0 deg
Nominal Tip clearance in m	0.1
Blade pitch at r/R	0.75
Angle of attack α in deg	-10 < α < 22
Flap position β in deg	0, 20, 35
Thrust coefficient C_T	0.07 < C_T < 0.3

TAB 4. Overview of test conditions.

Another variable that is changed between the individual operating points is the thrust. This should be the same for all three propulsion units within one OP. Since the rotational speed must kept constant within an OP, the propeller blades are pitched for this purpose. In the planned campaign a wide range of thrust levels will be tested. The thrust coefficient

$$C_T = \frac{T}{\rho\ n^2\ D^4} \tag{3}$$

can be used to compare the configurations. A total of seven thrust coefficients in the range of $0.07 < C_T < 0.3$ will be investigated, with with sufficient overlap between the three configurations.

The three co-rotating propulsion units are on a separate carrier that can be traversed and pitched relative to the wing in all degrees of freedom. This enables a thorough investigation of propeller positions. The axial distance of the propeller plane to the leading edge of the wing ranges from $0 < x/D < 1$ and the vertical position from $-0.25 < z/D < 0.25$. The spanwise distance from propeller is only limited by the propeller diameter and the wind tunnel. The inclination angle can easily be modified. In the upcoming test campaign only an angle of zero is studied.

4. CONCLUSION

DEP offers the possibility to share the power required for flight to small drive units installed e.g. along the span. This approach and the resulting possible beneficial aerodynamic effects and weight savings can reduce CO_2 emissions. Therefore, in addition to numerical investigations, comprehensive experimental studies are necessary to identify positive but also negative effects of DP. Especially for high-lift configurations, a sound and reliable prediction of the aerodynamic effect is not yet available. The overall objective of this design is to close this gap by providing high fidelity experimental data. Key design parameters that determine the sensitivity of positive and negative aerodynamic effects will be identified and quantified. The results will significantly increase the conceptual and preliminary design knowledge for DEP/DP driven aircraft.

Due to the large number of possible parameter variations, the design provides the opportunity to obtain new high-quality measurement data. The results obtained may ultimately provide better predictions for future designs and further limit the parameter space. The propeller generates disturbances upstream of the wing in various length scales, which have influence on the high-lift performance. Experimental data will be generated which characterises the stall behaviour of the airfoil. Both quasi-steady-state interactions and unsteady effects can be studied with the described measurement techniques. The isolated measurement of the integral forces on the centre section only allows mitigation of wind tunnel interference. Due to the different design and dimension of the propeller sets, but with the same thrust coefficients and blade tip speeds, comparable data for different advance ratios are produced. The experimental techniques selected allow quantifying the full temporal mean state of the airfoil flow in terms of flow patterns, pressure distribution and laminar-turbulent transition. The obtained data can be used to validate future numerical simulations in order to improve the design of future DEP concepts.

5. ACKNOWLEDGEMENT

This project has received funding from the Clean Sky 2 Joint Undertaking (JU) under grant agreement No 101007567. The JU receives support from the European Union's Horizon 2020 research and innovation programme and the Clean Sky 2 JU members other than the Union.
The authors would like to emphasise CIRA for their part in this experiment.

Contact address:

j.oldeweme@ifas.tu-braunschweig.de

References

[1] Hyun D. Kim, Aaron T. Perry, and Phillip J. Ansell. A review of distributed electric propulsion concepts for air vehicle technology. In *2018 AIAA/IEEE Electric Aircraft Technologies Symposium*. American Institute of Aeronautics and Astronautics. DOI: 10.2514/6.2018-4998.

[2] Stanislav Karpuk and Ali Elham. Influence of novel airframe technologies on the feasibility of fully-electric regional aviation. 8(6). DOI: 10.3390/aerospace8060163.

[3] T.C.A. Stokkermans. *Aerodynamics of Propellers in Interaction Dominated Flowfields: An Application to Novel Aerospace Vehicles*. PhD thesis, Delft University of Technology, 2020. DOI: 10.4233/uuid:46178824-bb80-4247-83f1-dc8a9ca7d8e3.

[4] Tomas Sinnige. *Aerodynamic and Aeroacoustic Interaction Effects for Tip-Mounted Propellers: An Experimental Study*. PhD thesis, Delft University of Technology, 2018. DOI: 10.4233/uuid:214e1e9a-c53e-47c7-a12c-b1eb3ec8293b.

[5] Tomas Sinnige, Robert Nederlof, and Nando van Arnhem. Aerodynamic performance of wingtip-mounted propellers in tractor and pusher configuration. In *AIAA AVIATION 2021 FORUM*. American Institute of Aeronautics and Astronautics. DOI: 10.2514/6.2021-2511.

[6] Reynard de Vries, Nando van Arnhem, Tomas Sinnige, Roelof Vos, and Leo L.M. Veldhuis. Aerodynamic interaction between propellers of a distributed-propulsion system in forward flight. 118:107009. DOI: 10.1016/j.ast.2021.107009.

[7] Karen A. Deere, Sally Viken, Melissa Carter, Jeffrey K. Viken, Michael Wiese, and Norma Farr. Computational analysis of powered lift augmentation for the LEAPTech distributed electric propulsion wing. In *35th AIAA Applied Aerodynamics Conference*. American Institute of Aeronautics and Astronautics. DOI: 10.2514/6.2017-3921.

[8] Karen A. Deere, Sally Viken, Melissa B. Carter, Jeffrey K. Viken, David E. Cox, Michael R. Wiese, and Norma L. Farr. Computational component build-up for the x-57 maxwell distributed electric propulsion aircraft. In *2018 AIAA Aerospace Sciences Meeting*. American Institute of Aeronautics and Astronautics. DOI: 10.2514/6.2018-1275.

[9] Michael D. Patterson. *Conceptual Design of high-lift propeller systems for small electric aircraft*. PhD thesis, Georgia Institute of Technology, 2016.

[10] Leo Veldhuis. *Propeller Wing Aerodynamic Interference*. PhD thesis, Delft University of Technology, 2005.

[11] Jan-Hendrik Krone and Jens Friedrichs. Generation of intake distortion due to angle of attack for a high bypass turbofan model. In *Volume 1: Advances in Aerospace Technology*, page V001T01A064. American Society of Mechanical Engineers. DOI: 10.1115/IMECE2014-38097.

[12] A. Pagano. Aerofoil selection and spanwise placement in aerodynamic design and optimization of tiltrotor blades. 39th European Rotorcraft Forum, Moscow, Russia, 2013.

[13] A. Pagano. Aerodynamic shape optimization of tiltrotor blades equipped with continuous morphing aerofoils. 41st European Rotorcraft Forum, Munich, Germany, 2015.

[14] M. Bauer, D. Wulff, and J. Friedrichs. Bürgernahes flugzeug: testing technology for the high power propeller of a wind tunnel model. 7(2):225–239. DOI: 10.1007/s13272-016-0183-6.